Radiative Cooling, Latent Heating, and Cloud Ice in the Tropical Upper Troposphere

ADAM B. SOKOL[a] AND DENNIS L. HARTMANN[a]

[a] *Department of Atmospheric Sciences, University of Washington, Seattle, Washington*

ABSTRACT: The radiative cooling rate in the tropical upper troposphere is expected to increase as climate warms. Since the tropics are approximately in radiative–convective equilibrium (RCE), this implies an increase in the convective heating rate, which is the sum of the latent heating rate and the eddy heat flux convergence. We examine the impact of these changes on the vertical profile of cloud ice amount in cloud-resolving simulations of RCE. Three simulations are conducted: a control run, a warming run, and an experimental run in which there is no warming but a temperature forcing is imposed to mimic the warming-induced increase in radiative cooling. Surface warming causes a reduction in cloud fraction at all upper-tropospheric temperature levels but an increase in the ice mixing ratio within deep convective cores. The experimental run has more cloud ice than the warming run at fixed temperature despite the fact that their latent heating rates are equal, which suggests that the efficiency of latent heating by cloud ice increases with warming. An analytic expression relating the ice-related latent heating rate to a number of other factors is derived and used to understand the model results. This reveals that the increase in latent heating efficiency is driven mostly by 1) the migration of isotherms to lower pressure and 2) a slight warming of the top of the convective layer. These physically robust changes act to reduce the residence time of ice at any particular temperature level, which tempers the response of the mean cloud ice profile to warming.

SIGNIFICANCE STATEMENT: Here we examine how the amount of condensed ice in part of the atmosphere—the tropical upper troposphere (UT)—responds to global warming. In the UT, the energy released during ice formation is balanced by the emission of radiation to space. This emission will strengthen with warming, suggesting that there will also be more ice. Using a model of the tropical atmosphere, we find that the increase in ice amount is mitigated by a reduction in the amount of time ice spends in the UT. This could have important implications for the cloud response to global warming, and future work should focus on how these changes are manifested across the distribution of convective cloud types.

1. Introduction

Ice clouds produced by tropical convection play an important role in Earth's climate yet remain a significant source of uncertainty in projections of climate change (Bony et al. 2015; Zelinka et al. 2017). Changes in the properties and abundance of deep convective cores and their associated anvil clouds could have wide implications for the tropical radiation budget and global climate (Zelinka et al. 2012; Hartmann 2016). Predicting these changes requires an understanding of complex dynamic, microphysical, and radiative processes that are difficult to observe and model. This complexity is evident in the Radiative–Convective Equilibrium Model Intercomparison Project (RCEMIP), in which different cloud-resolving models (CRMs) with nearly identical domains produce wildly different cloud climatologies and cloud responses to warming (Wing et al. 2020). While the radiative feedbacks associated with tropical convection remain difficult to constrain, recent work has advanced understanding of how warming may impact more specific aspects of convection,

including its large-scale organization (e.g., Coppin and Bony 2018), precipitation efficiency (e.g., Lutsko and Cronin 2018), and anvil cloud evolution (e.g., Gasparini et al. 2021). In this paper, we examine how warming may impact the mean profile of cloud ice amount.

The radiative–convective equilibrium (RCE) approximation provides a conceptual link between the formation of ice and the atmospheric radiative cooling rate Q_R. The formation of ice during convection releases latent heat, which is transported to the upper troposphere (UT) by deep convective plumes. This latent heating, along with the eddy heat flux convergence associated with the convection, constitutes the total convective heating. In RCE, convective heating is balanced by Q_R, which we can compute accurately for known temperature and moisture profiles.

Models of varying complexity predict that Q_R in the UT will increase with warming if the temperature profile approximately follows a moist adiabat. This result is supported by prior work using early general circulation models (Mitchell and Ingram 1992; Knutson and Manabe 1995), simple spectral models (Jeevanjee and Fueglistaler 2020), and modern line-by-line models (Jeevanjee and Fueglistaler 2020). Jeevanjee and Romps (2018) showed that the radiative flux divergence (W m^{-2} K^{-1} in temperature coordinates) at any particular temperature is unaffected by surface warming in simulations

of RCE. But warming drives isotherms to lower pressures, where the ambient air is less dense. This produces an increase in Q_R (K day^{-1}), since Q_R is inversely related to density. Hartmann et al. (2022, manuscript submitted to *J. Climate*) used the cooling-to-space approximation to show that emission from the atmosphere is purely a function of temperature and relative humidity, but as the surface warms and the emission moves to a lower pressure, the transmission to space increases, which allows Q_R to increase. If the temperature profile follows a moist adiabat, Q_R preferentially increases at the anvil cloud level, causing the Q_R profile to become more top-heavy.

This paper seeks to understand how the warming-driven increase in Q_R affects the mean profile of cloud ice amount in an RCE framework. Doing so requires us to examine the connection between radiative cooling, latent heating, and the ice mass mixing ratio q_i in the UT. In section 2, we describe a set of CRM simulations that allow us to examine how the atmosphere responds to an increase in Q_R with and without a corresponding change in surface temperature. This will show that the q_i response to warming is tempered by an increase in the efficiency by which ice imparts latent heat to the UT. To understand this change, we develop a mathematical expression for the ice-related latent heating rate and use it to diagnose the CRM results (sections 3 and 4). This will show that the increased efficiency of latent heating is caused by the migration of isotherms to lower pressures and by the slight warming of the top of the convective layer. We discuss and contextualize these results in section 5.

2. Cloud-resolving model simulations

We conduct RCE simulations using the System for Atmospheric Modeling (SAM; Khairoutdinov and Randall 2003) with RRTM radiative transfer code (Iacono et al. 2000; Mlawer et al. 1997). The model domain is 96 km × 96 km with 2-km horizontal resolution and periodic lateral boundaries. Because this small domain precludes convective aggregation, we can be confident that changes in the degree of aggregation do not impact our results. The vertical grid has 128 levels with variable spacing. The spacing is 50 m near the surface, smoothly increases to ~300 m by 5 km, and increases again between 25 and 39 km to a maximum spacing of 1 km. Gravity waves are dampened by a sponge layer extending upward from 27 km. Sea surface temperature (SST) is fixed and uniform, there is no rotation, and insolation follows a fixed diurnal cycle corresponding to 1 January at the equator. We use the Predicted Particle Properties (P3) bulk microphysics scheme (Morrison and Milbrandt 2015), which has a single ice-phase hydrometeor category with four prognosed variables: total ice mass, total ice number, rime mass, and rime volume. Because P3 has only one ice category, we do not differentiate between precipitating and nonprecipitating ice. We use the term "cloud ice" to refer to all ice-phase hydrometeors and the symbol q_i to denote the total ice mass mixing ratio.

Three simulations are conducted:

1) *con300*: a 350-day control run with 300-K SST,
2) *con305*: a 350-day warming run with 305-K SST, and
3) *force300*: an experimental run with 300-K SST and a forced cooling F intended to mimic the upper-tropospheric Q_R response to warming. This run is branched from con300 at day 150 and integrated for another 150 days. Note that F is sinusoidal in pressure coordinates with positive (cooling) and negative (warming) lobes in the ranges 250–550 and 550–850 hPa, respectively, and a maximum amplitude of 0.26 K day^{-1} (Fig. 1a). Because of its sinusoidal structure, F has a mass integral of zero and thus no direct effect on the column-integrated cooling rate. We conducted an additional run in which F consisted only of its upper lobe, but there were no significant differences in the upper-tropospheric quantities of interest.

The time-averaged results shown in the following sections reflect the last 75 days of each model run.

In equilibrium, the convective heating rate must balance the sum of Q_R and F, which we denote as Q_{R+F}. The solid lines in Figs. 1b and 1c show Q_{R+F} for each run. Because there is no forcing in con300 and con305, Q_{R+F} is just equal to Q_R in those runs and is larger in con305 for the reasons discussed in section 1. The increase in Q_R with warming is limited to temperatures above ~220 K, since the Q_R profile is constrained to decrease at colder temperatures due to the scarcity of water vapor (Hartmann and Larson 2002). In force300, Q_R (dashed red line) is similar to that in con300, reflecting the fact that the two runs have equal SST and thus very similar temperature and moisture profiles. But because F is nonzero in force300, upper-tropospheric Q_{R+F} is more like that in con305, especially when viewed in temperature coordinates (Fig. 1c). So while the temperature, moisture, and Q_R profiles in force300 match its 300-K SST, the total cooling "experienced" in the UT corresponds to a SST of 305 K. This is exactly the intent of the temperature forcing and will allow us to compare the atmosphere's response to increased Q_{R+F} in the presence and absence of SST warming. An implication of this approach is that F does not capture the warming-driven shift of the Q_R profile to lower pressures (Fig. 1b).

The increase in upper-tropospheric Q_{R+F} in con305 and force300 must be balanced by an increase in convective heating. We can examine the energy budget of the UT to better understand how this is achieved. The thermodynamic variable used for this budget analysis and throughout the rest of the paper is the liquid–ice static energy:

$$s = c_p T + gz - Lq_l - L_s q_i, \tag{1}$$

where C_p is the specific heat of dry air at constant pressure, T is temperature, g is the gravitational acceleration, q_l is the mass mixing ratio of all liquid condensate, and L and L_s are the latent heats of vaporization and sublimation, respectively. The term s is the prognostic thermodynamic variable in SAM and is exactly conserved by the model's governing equations. It is informative to use s for our analysis because it is
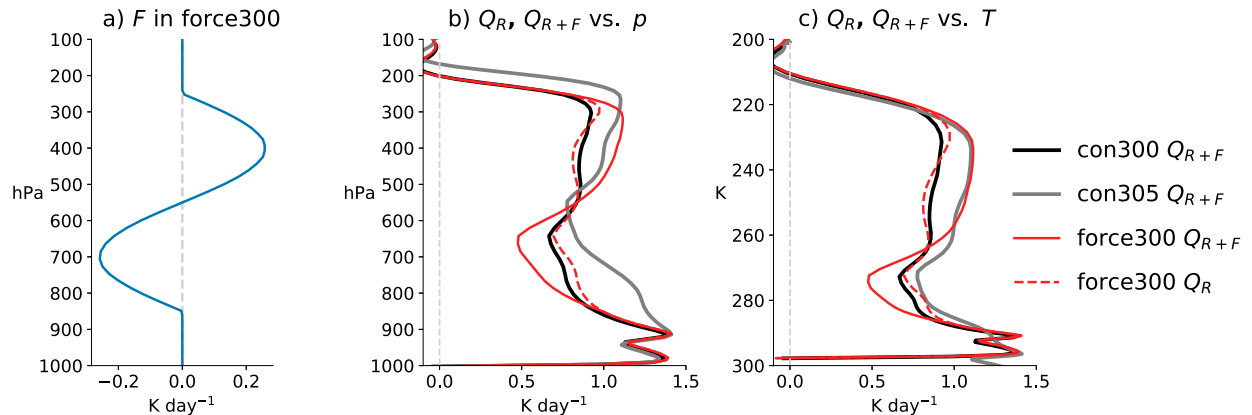
FIG. 1. (a) The forced cooling rate F applied in force300. (b) Dashed red line: the radiative cooling rate Q_R in force300. Solid lines: the combined radiative and forced cooling rate Q_{R+F} in all three simulations. (c) As in (b), but as a function of temperature. Note that Q_R and Q_{R+F} are equal in con300 and con305. The radiative cooling rates are for all-sky conditions.

approximately conserved during moist adiabatic processes and is therefore unaffected by phase changes.

Figure 2a shows the model-computed tendencies of s due to Q_{R+F}, advection, and latent heating. These three tendencies, along with a very small diffusive tendency (not shown), form a closed energy budget. The advective tendency is negative because s increases with height, meaning that convective plumes deposit low-s air from the surface into the high-s UT. Because there is no large-scale vertical motion in these runs, the advective tendency is comprised solely of the heating by resolved eddies. The convective heating rate is thus equal to the sum of the advective and latent heating tendencies.

Figure 2a indicates that both the latent and advective components of the s budget strengthen in response to the increase in Q_{R+F} in con305 and force300. The increase in latent heating dominates, so the convective heating rate increases as a result. This increase in latent heating must be associated with changes

in ice, since liquid condensate is scarce or nonexistent at temperatures below ~245 K. To formally distinguish the ice-related latent heating from the total latent heating, we define $\dot{s}_{\text{ice}}$ as the latent heating tendency of s due to ice alone. To better conceptualize $\dot{s}_{\text{ice}}$, let us consider a saturated air parcel rising in a deep convective plume. Once the freezing level is surpassed, ice accumulates via freezing, vapor deposition, and/or new nucleation. This releases latent heat, which warms the parcel but does not change s, since s is conserved during phase changes. For as long as the ice remains with the parcel, there is the possibility that it sublimates and consumes the latent heat released during its formation. But if the ice sediments out of the parcel, that latent heat is irreversibly left behind, and as shown by Eq. (1), s increases because q_i has decreased. The important point here is that the latent heating of s results not from the formation of ice but from its irreversible sedimentation later on. This can be expressed mathematically as
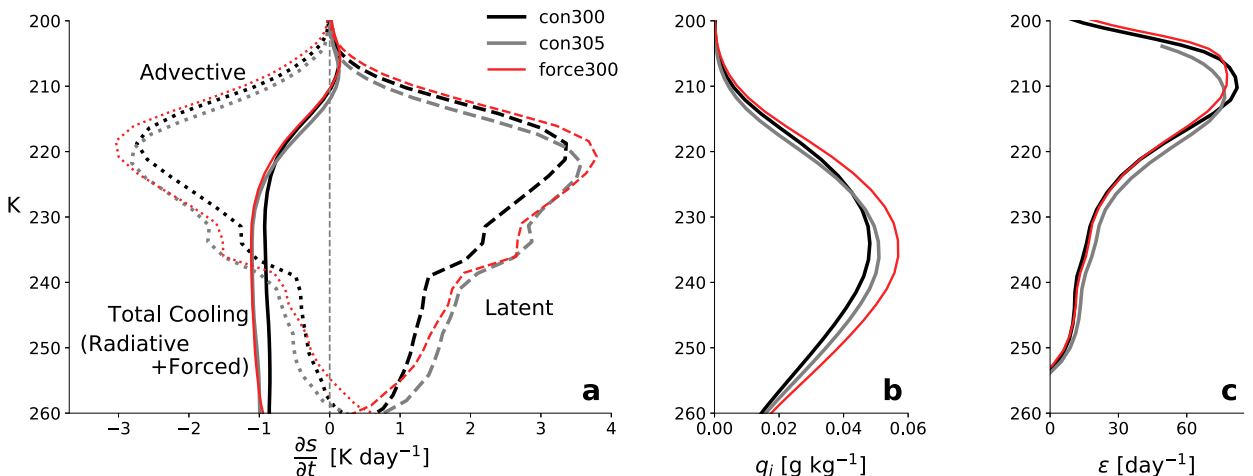

FIG. 2. (a) Tendencies of the liquid–ice static energy s due to latent heating (dashed), advection (dotted), and radiative (solid) and forced cooling Q_{R+F}. Tendencies are divided by C_p so that they have units of K day^{-1}. The sum of the three tendencies is approximately equal to zero in equilibrium, since the diffusive tendency is small. (b) Domain-averaged ice mass mixing ratio q_i. (c) Latent heating efficiency of ice, ϵ, given by Eq. (3).
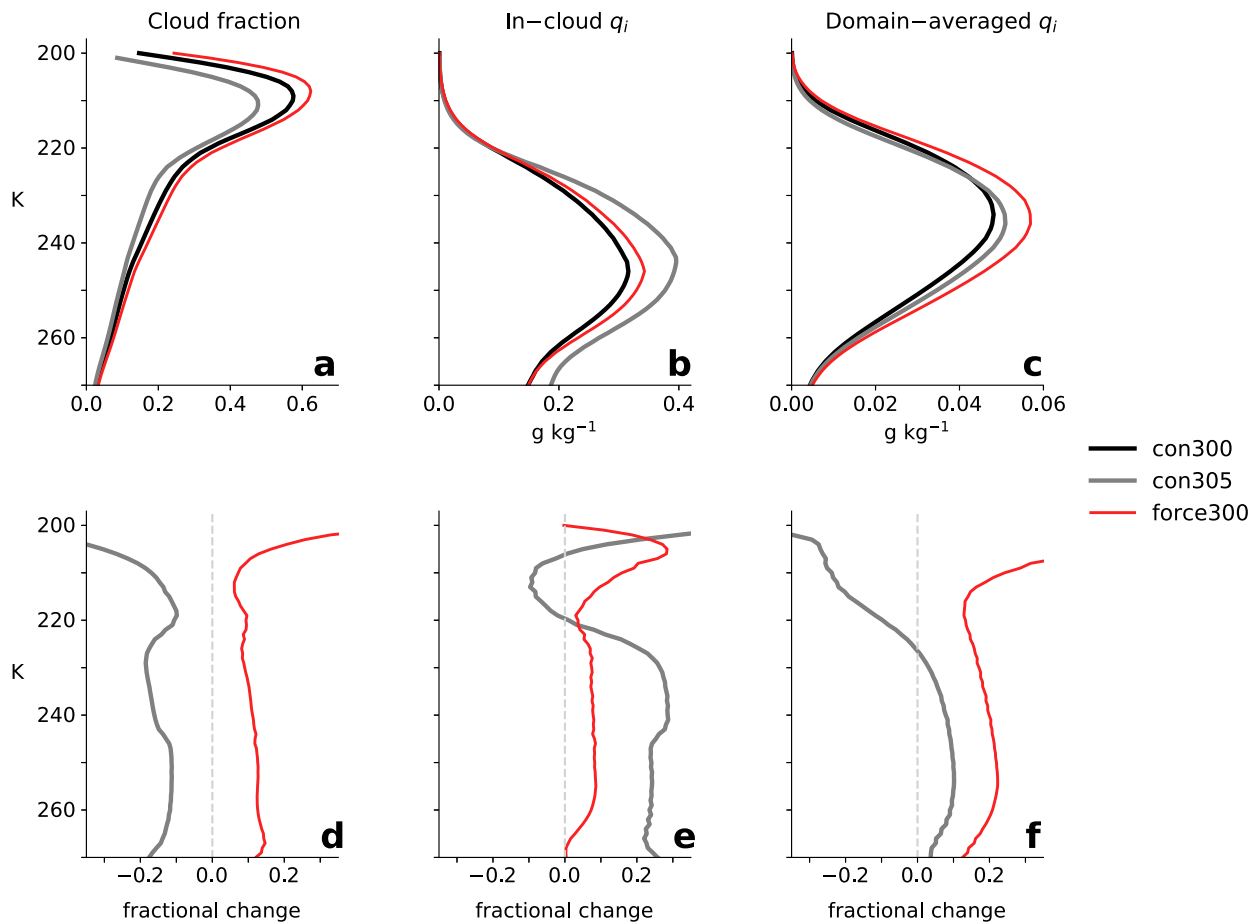
FIG. 3. (a) Cloud fraction, (b) in-cloud ice mixing ratio, and (c) domain-averaged ice mixing ratio as a function of temperature in the three simulations. (d)–(f) Fractional changes in each quantity with respect to con300. Model grid boxes are considered cloudy if the total condensate mixing ratio exceeds 10^{-5} kg kg^{-1} or 1% of the saturation vapor pressure of water, whichever is smaller.

$$\dot{s}_{\text{ice}} = - L_s \dot{q}_{i_{\text{sed}}}, \qquad (2)$$

where $\dot{q}_{i_{\text{sed}}}$ is the tendency of q_i due to sedimentation.

Because $\dot{s}_{\text{ice}}$ is determined by the net ice sedimentation rate rather than q_i itself, the relative differences in $\dot{s}_{\text{ice}}$ between the three simulations are not necessarily reflected in their domain-averaged q_i profiles. This is evident in Fig. 2b. The q_i value is highest in force300 despite the fact that there is more latent heating in con305 over much of the same temperature range. In con305, the fractional increase in $\dot{s}_{\text{ice}}$ relative to con300 far exceeds that in q_i throughout most of the UT. In force300, while the fractional changes in $\dot{s}_{\text{ice}}$ and q_i are not exactly equal, they are much more similar. This difference is encapsulated by what we define as the latent heating efficiency:

$$\epsilon \equiv \frac{\dot{s}_{\text{ice}}}{L_s q_i}. \qquad (3)$$

It is important that ϵ not be confused with the precipitation efficiency, as they are different in nature. As ϵ increases, a smaller mean q_i is needed to achieve a given amount of latent heating. Figure 2c shows profiles of ϵ for the three simulations.

At air temperatures exceeding 215 K, ϵ is nearly the same in con300 and force300 but is larger in con305, suggesting that ϵ increases with SST. As will be shown later, additional simulations with SSTs of 295, 310, and 315 K support this trend.

Changes in the domain-averaged q_i can be caused both by changes in cloud fraction and by changes in the in-cloud ice amount. These two factors have important implications for both the top-of-atmosphere energy budget and atmospheric radiative heating rates, which have been shown to play an important role in the circulation response to warming (Voigt et al. 2019). In con305, ice cloud fraction is lower at any particular temperature than in con300 but the in-cloud q_i is higher on average (Fig. 3). The fractional increase in in-cloud q_i dominates the decrease in cloud fraction for $T > 224$ K, and so the domain-averaged q_i increases there. This results primarily from an increase in the amount of ice within deep convective cores; if we were to exclude the 2% of the model domain with the highest column-integrated ice water path (IWP) from the calculation of domain-averaged q_i, then q_i would actually decrease with warming at most upper-tropospheric temperature levels. Thus, it is the increase in q_i in the iciest parts of the atmosphere that is

responsible for the increase in domain-averaged q_i at fixed temperature. In contrast, the large increase in domain-averaged q_i in force300 comes mostly from an increase in cloud fraction, with a small increase in in-cloud q_i playing a lesser role. These differences make sense: as SSTs warm, the troposphere deepens and warms at its base, and convective updrafts accumulate a greater amount of condensate before reaching any particular isotherm in the upper troposphere. Because there is no warming in force300, any significant increase in domain-averaged q_i must come from changes in cloud fraction.

Cloud changes can be further understood by examining probability density functions (PDFs) of IWP, shown in Fig. 4a. The PDFs are computed from instantaneous 2D snapshots taken at 6-h intervals for the final 75 days of each simulation. None of these snapshots contain grid cells with zero IWP, likely because the domain is relatively small and is easily covered by ice spreading out from convective regions. Because true clear-sky conditions do not occur, altering the IWP distribution is a zero-sum game: differences in the PDFs at one IWP must be compensated for by differences at another IWP rather than by differences in total cloud coverage. In con305, SST warming reduces the coverage of clouds with $\log_{10}$ IWP between 20.3 and 3.5 (Fig. 4b), which include convective cores, detrained anvil clouds, and other thin cirrus (Sokol and Hartmann 2020). This reduction is compensated for by an increase in the area with $\log_{10}$ IWP between -2 and -0.3, which is as close as it gets to clear-sky conditions in these simulations. In essence, warming shifts the IWP distribution toward lower values, and the mean IWP decreases by 6% as a result (Fig. 4a). This may seem counterintuitive given the increase in domain-averaged q_i at fixed temperature shown in Fig. 2b, but the pressure and density at a fixed temperature decrease with SST warming, and so the same q_i (kg kg^{-1}) corresponds to a smaller ice water content (kg m^{-3}), which is the quantity used to compute IWP. In force300, the IWP changes are reversed. The frequency of high IWPs increases at the expense of low IWPs, which shifts the distribution toward higher values and increases the mean IWP by 23%.

In this brief overview of the CRM results, we have found that RCE requires $\dot{s}_{ice}$ to increase in response to an increase in Q_{R+F} whether it is driven by SST warming or an imposed temperature forcing. On the other hand, latent heating efficiency is largely unaffected by the temperature forcing but increases with warming. This allows the q_i profiles in con305 and force300 to differ substantially even at temperatures where $\dot{s}_{ice}$ is equal. In con305, an increase in convective core q_i drives the slight increase in domain-averaged q_i, while in force300 the much larger increase in domain-averaged q_i is due mainly to greater cloudiness. These results raise some interesting questions. What is the relationship between latent heating and q_i? Why does the latent heating efficiency increase with SST? And what can this tell us about the q_i response to warming? We address these questions in the following sections.

3. A theoretical model for latent heating

Our goal in this section is to develop an expression relating $\dot{s}_{ice}$ to q_i. Equation (2) defines $\dot{s}_{ice}$ in terms of $\dot{q}_{i_{sed}}$, which is the sedimentation tendency of q_i equal to
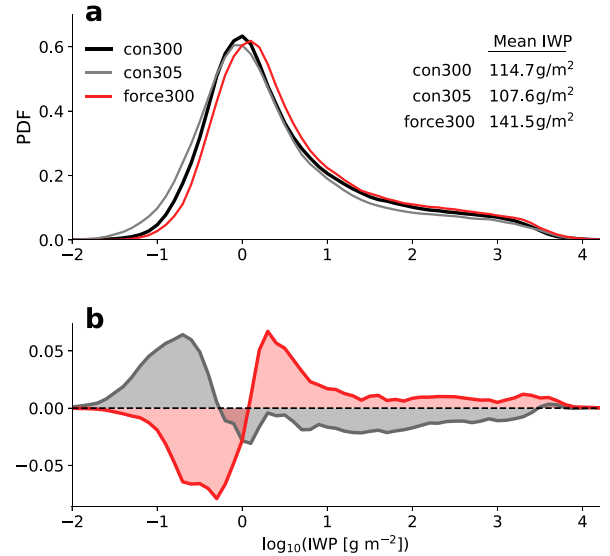

FIG. 4. (a) Probability density functions (PDFs) of $\log_{10}$ IWP for each simulation. (b) Changes in the IWP PDF with respect to con300.

$$\dot{q}_{i_{sed}} = -\frac{1}{\rho} \frac{\partial F_{sed}}{\partial z}, \qquad (4)$$

where ρ is the air density and F_{sed} is the sedimentation ice flux. In the P3 scheme, this is given by

$$F_{sed} = \rho q_i f V_m, \qquad (5)$$

where V_m is the mass-weighted ice crystal terminal fall speed calculated following Mitchell and Heymsfield (2005); f is an air density modification to V_m that, following Heymsfield et al. (2007), is given by $(\rho_0/\rho)^{0.54}$, where ρ_0 is a reference density. Substituting in for f in (5) gives $F_{sed} = \rho_0^{0.54}\rho^{0.46}q_i V_m$. Combining this with (2) and (4) yields

$$\dot{s}_{ice} = \frac{k}{\rho} \frac{\partial}{\partial z}\left(\rho^{0.46} q_i V_m\right), \qquad (6)$$

where $k = L_s \rho_0^{0.54}$. Expanding the derivative gives

$$\dot{s}_{ice} = \frac{k}{\rho^{0.54}}\left(0.46 q_i V_m \frac{\partial\ln\rho}{\partial z} + q_i \frac{\partial V_m}{\partial z} + V_m \frac{\partial q_i}{\partial z}\right). \qquad (7)$$

Using the ideal gas law $p = \rho R_d T_v$ and hydrostatic balance $\partial p/\partial z = -\rho g$, it can be shown that

$$\frac{\partial\ln\rho}{\partial z} \approx \frac{1}{T}\left(\Gamma - \frac{g}{R_d}\right), \qquad (8)$$

where Γ is the lapse rate and R_d is the gas constant for dry air. Here we have assumed that the virtual temperature T_v is approximately equal to the absolute temperature T, which is a good approximation over the range of temperatures that we will consider. Combining (7) and (8) and replacing $\partial/\partial z$ with $-\Gamma\partial/\partial T$ gives

$$\dot{s}_{\text{ice}} = \frac{k}{\rho^{0.54}} \left[\Gamma \left(\frac{0.46 V_m q_i}{T} - q_i \frac{\partial V_m}{\partial T} - V_m \frac{\partial q_i}{\partial T} \right) - \frac{0.46 c q_i V_m}{T} \right],$$
(9)

where $c = g/R_d$. The conversion to temperature coordinates simplifies the comparison of simulations with different SSTs because the temperature at which Q_R falls toward zero—which is also the top of the convective layer—is approximately fixed (Hartmann and Larson 2002). This is illustrated in Fig. 1c, in which the Q_R and Q_{R+F} curves collapse onto one another at ~220 K.

Equation (9) is useful because it allows us to calculate the domain-averaged $\dot{s}_{\text{ice}}$ profile given profiles of T, ρ, q_i, and V_m. If we convert these profiles to temperature coordinates, we can calculate $\partial q_i/\partial T$ and $\partial V_m/\partial T$, which we denote as q_i' and V_m', respectively. Then, using the total differential of (9), we can attribute changes in $\dot{s}_{\text{ice}}$ at some fixed T to changes in six different variables:

$$\Delta \dot{s}_{\text{ice}} \approx \Delta \rho \frac{\partial \dot{s}_{\text{ice}}}{\partial \rho} + \Delta \Gamma \frac{\partial \dot{s}_{\text{ice}}}{\partial \Gamma} + \Delta V_m \frac{\partial \dot{s}_{\text{ice}}}{\partial V_m} + \Delta V_m' \frac{\partial \dot{s}_{\text{ice}}}{\partial V_m'}$$

$$+ \Delta q_i \frac{\partial \dot{s}_{\text{ice}}}{\partial q_i} + \Delta q_i' \frac{\partial \dot{s}_{\text{ice}}}{\partial q_i'}.$$
(10)

Here, ΔX denotes the change in X at fixed T relative to some baseline. Expressions for the partial derivatives can be determined analytically from (9) and are provided in appendix A. Equation (10) is an accurate approximation of $\Delta \dot{s}_{\text{ice}}$ over the range of atmospheric states produced by the three model runs (appendix B).

4. Application to model simulations

We can now use Eq. (10) to understand the differences in $\dot{s}_{\text{ice}}$ between the three simulations. To do so, we must evaluate each term on the right-hand side for con305 and force300, using con300 as a baseline. The value of each term can be interpreted as the contribution of that variable to the total change in $\dot{s}_{\text{ice}}$ at some particular T. The model provides hourly profiles of domain-averaged T, ρ, q_i, and F_{sed} in height coordinates. For each time step, we compute Γ and compute the q_i-weighted V_m as $F_{\text{sed}}/(f\rho q_i)$, which follows from Eq. (5). We then convert the vertical grid to temperature coordinates using the time- and domain-averaged T at each vertical level, interpolate the profiles onto a common T grid, and calculate q_i' and V_m'. We use output from con300 to compute the partial derivatives in Eq. (10), and the Δ terms are computed for con305 and force300 with respect to con300.

Figure 5 shows the results of this procedure, with each colored line representing one of the six terms on the right-hand side of Eq. (10). The bold black lines, which show $\Delta \dot{s}_{\text{ice}}$, are equal to the sum of the six individual terms and correspond closely to the differences in the latent heating profiles shown in Fig. 2a. The profiles have been normalized by C_p so that they are in K day^{-1}. If a profile is near the zero line, then the

variable it represents does not change significantly at that T and therefore has little impact on $\dot{s}_{\text{ice}}$.

In the following sections, we discuss each variable and its relevance to changes in $\dot{s}_{\text{ice}}$ before synthesizing the results with a discussion of latent heating efficiency. All changes (e.g., increases and decreases) mentioned in this section are with respect to con300 unless stated otherwise. It is important to remember that $\dot{s}_{\text{ice}}$ is only equal to the total latent heating of s when the effects of liquid condensate are negligible. In our model runs, $\dot{s}_{\text{ice}}$ accounts for 90% or more of the total latent heating at temperatures colder than 245 K, and we therefore restrict our analysis to that range.

a. Density and lapse rate

We begin by discussing ρ and Γ together because their values at any particular T are both fundamentally linked to SST. This linkage arises from the fact that the tropical temperature profile is dynamically constrained to be close to a moist adiabat originating from the boundary layer (Sobel et al. 2001), and the temperature of the boundary layer is determined by the SST. Since con300 and force300 have the same SST, they also have similar T profiles and therefore similar ρ and Γ at any particular T. Consequently, in force300 the ρ and Γ contributions to $\Delta \dot{s}_{\text{ice}}$ (blue and orange lines in Fig. 5b, respectively) are negligible.

On the other hand, SST warming in con305 drives isotherms upward toward lower pressures, and the ρ at any particular T decreases as a result. Since $\dot{s}_{\text{ice}}$ and ρ are inversely related in Eq. (9), the decrease in ρ acts to increase $\dot{s}_{\text{ice}}$, as evidenced by the positive values of the ρ term (blue line) in Fig. 5a. The physical interpretation of this ρ effect is straightforward: ice crystals fall faster at lower air densities because drag is reduced. As ρ decreases, ice crystals are quick to sediment out of a parcel and leave their latent heat behind. Mathematically, the ρ effect stems from the density modification f applied to the ice crystal fall speed, and the magnitude of the ρ effect is therefore sensitive to the formulation of f. But insofar as ρ and fall speed are inversely related, the sign of the ρ effect is robust.

Changes in Γ in con305 act to reduce $\dot{s}_{\text{ice}}$, as shown by the orange line in Fig. 5a. This, too, arises from the migration of isotherms to lower pressures with warming, which reduces the moist adiabatic lapse rate at any particular T. The pressure dependence of the moist adiabatic lapse rate is indirect, occurring by way of the saturation specific humidity. The reduction in Γ with warming causes our temperature range of interest to expand vertically in Cartesian space, which "stretches out" and weakens the sedimentation flux divergence, reducing $\dot{s}_{\text{ice}}$. The sign of the Γ effect seems robust considering that an increase in static stability (decrease in Γ) with warming has long appeared in observations and models (Knutson and Manabe 1995; Zelinka and Hartmann 2010, 2011; Bony et al. 2016). Its magnitude, especially in the uppermost UT, could be influenced by the model's representation of ozone. Note that Γ could also be sensitive to model resolution if resolution impacts the entrainment rate, since entrainment modifies the RCE temperature profile (Zhou and Xie 2019).
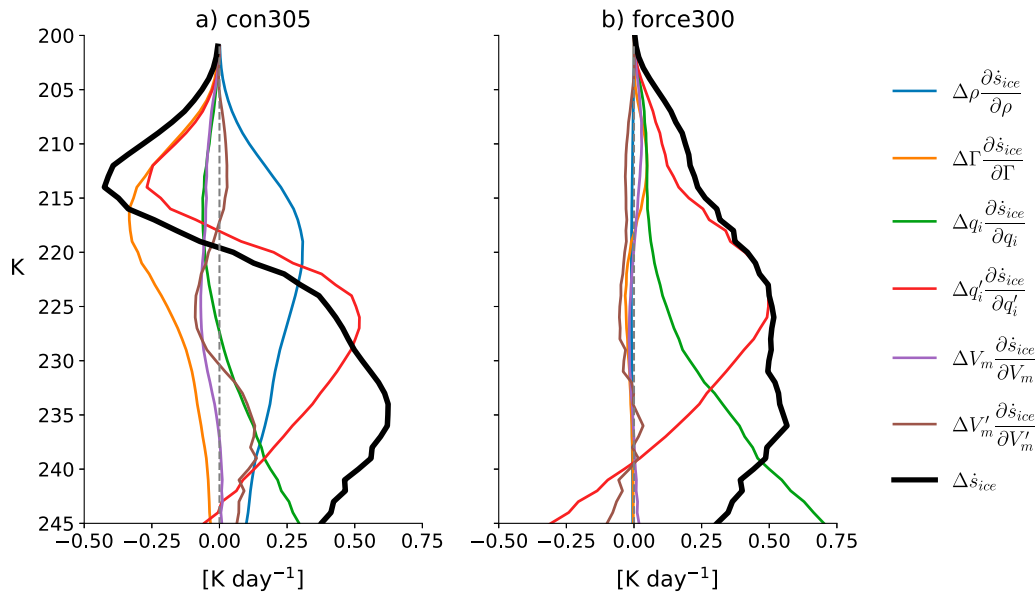
FIG. 5. Profiles of each term in Eq. (10) for (a) con305 and (b) force300. The terms are normalized by C_p so that they are in K day^{-1}. Black lines show the total $\Delta\dot{s}_{\text{ice}}$ relative to con300, which is equal to the sum of the six individual terms and corresponds to the differences in the latent heating tendencies in Fig. 2a.

The arguments in this section, grounded in first principles, tell us that the ρ and Γ effects push $\dot{s}_{\text{ice}}$ in opposing directions as SST warms. Ice crystals fall faster but must travel a greater distance from one isotherm to the next. The combined effect of ρ and Γ, which is relatively small compared to their individual effects, is negative at temperatures below 220 K and positive at warmer temperatures, with a positive mass integral between 200 and 245 K. Thus, if all else is equal, warming causes the $\dot{s}_{\text{ice}}$ profile to increase in magnitude and shift slightly toward warmer temperatures.

b. Ice crystal fall speed

We turn now to V_m and V'_m. Unlike ρ and Γ, V_m and V'_m do not have an obvious SST dependence that can be inferred from first principles, so we instead rely here on their prediction by the P3 microphysics scheme. In P3, V_m is determined following Mitchell and Heymsfield (2005) and depends on several microphysical quantities, including ice particle density. Ice density is predicted from the scheme's prognostic ice variables and accounts for the effects of riming, which is critical for the simulation of certain convective structures (Morrison et al. 2015). This makes P3 well suited for the present analysis compared to schemes that sort ice particles into predefined categories with prescribed fall speeds. Changes in V_m between the three simulations reflect changes in ice microphysics and do not necessarily correspond to changes in the *actual* fall speed, since we have separated V_m from its air density modification factor f.

In force300, the V_m and V'_m effects on $\dot{s}_{\text{ice}}$ (purple and brown lines in Fig. 5b, respectively) are negligible, indicating that changes in ice microphysical properties cannot explain the increase in latent heating. In con305, the V_m and V'_m

effects are large enough to warrant discussion but are still relatively small compared to the other terms. The value of V_m increases (becomes less negative) throughout the UT, which acts to reduce $\dot{s}_{\text{ice}}$ above the level of maximum q_i (234 K) and enhance $\dot{s}_{\text{ice}}$ below. The V'_m effect has a more complicated vertical structure and is largest between 235 and 240 K, where a steepening of the V_m profile strengthens the sedimentation flux divergence and enhances $\dot{s}_{\text{ice}}$.

Understanding the slight differences in V_m and V'_m between our three simulations requires an in-depth analysis of their microphysics. We forgo such analysis here, since the V_m and V'_m effects are relatively small in both con305 and force300, and neglecting them produces only minor changes in $\Delta\dot{s}_{\text{ice}}$. Moreover, the insights gained from such an analysis would be specific to the P3 microphysics scheme and the V_m parameterization it employs. The parameterization of V_m is an obvious source of uncertainty in our results, and while the small size of the V_m and V'_m effects alleviates some of this uncertainty, it is possible that a different fall speed parameterization could produce very different results, although this would likely require large microphysical changes. The importance of ice fall speed in the tropical energy budget—underscored by the mere presence of V_m and V'_m in Eq. (9) and by a large body of research (e.g., Grabowski et al. 2000; Mitchell et al. 2008; Sanderson et al. 2008)—is worthy of further study.

c. Cloud ice

The two remaining terms in Eq. (10) are the q_i and q'_i terms, shown respectively by the green and red lines in Fig. 5. In force300, the increase in q_i acts to increase $\dot{s}_{\text{ice}}$ at all T. The q_i effect is largest at warmer temperatures, where the absolute
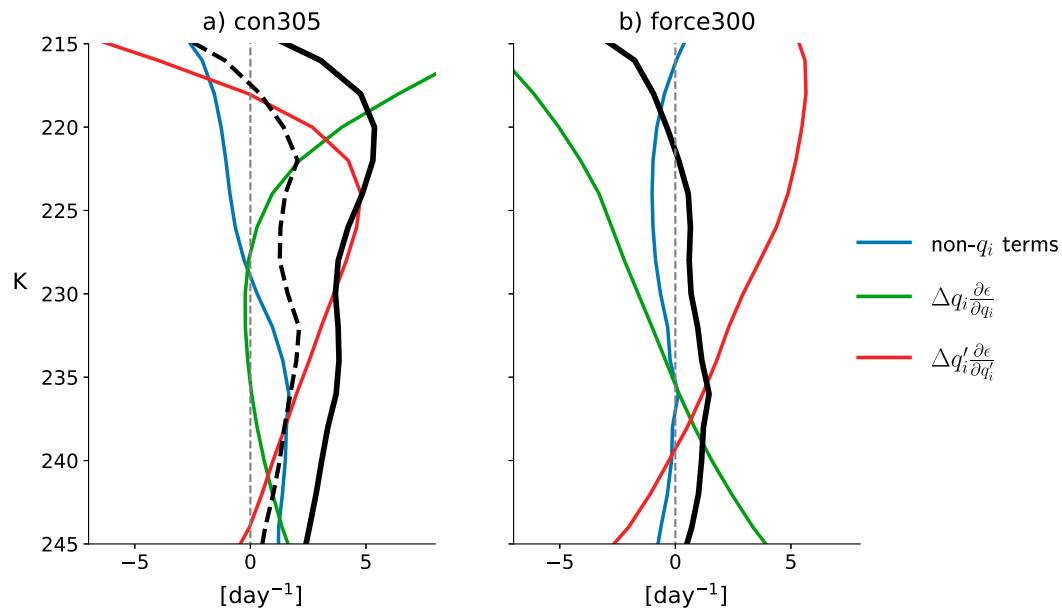
FIG. 6. Contributions of non-q_i factors (blue), q_i (green), and q_i' (red) to changes in the latent heating effi-
ciency ϵ relative to con300 in (a) con305 and (b) force300. Bold black lines show the total $\Delta\epsilon$, which is equal to
the sum of the three colored lines and corresponds to the differences in the ϵ profiles in Fig. 2c. The dashed
black line in (a) shows $\Delta\epsilon$ for a modified con305 scenario in which the q_i profile was shifted toward colder tem-
peratures by 1 K. Non-q_i terms include ρ, Γ, V_m, and V_m'.

change in q_i is greatest and where $\dot{s}_{\text{ice}}$ is especially sensitive to
changes in q_i because V_m is large. The q_i' effect is also signifi-
cant in force300 and reflects a general steepening of the q_i
profile, which causes q_i' at any particular T to increase in mag-
nitude but retain the same sign. If all else is equal, this acts to
enhance latent heating above the level of maximum q_i and
hinder it below. The q_i' effect dominates the total change in
$\dot{s}_{\text{ice}}$ at cold temperatures, whereas the q_i effect dominates at
warmer temperatures.

In con305, the q_i and q_i' effects have a more complex vertical
structure. This is due to a slight (1-K) warming of the top of the
convective layer, which results from an increase in tropospheric
stability with SST (Zelinka and Hartmann 2011). As the top of
the convective layer warms, so does the upper extent of the q_i
profile, but the lower extent is tied to the freezing level and thus
does not warm in the same way. As a result, the q_i profile is ver-
tically squashed in temperature space toward warmer tempera-
tures. One consequence of this shift is that the q_i and q_i' effects
are both negative at low T. Between 215 and 225 K, the q_i'
effect increases rapidly with T and becomes larger in magnitude
than the q_i effect, which is still negative. This is significant
because it produces an increase in $\dot{s}_{\text{ice}}$ despite a decrease in the
amount of ice. The q_i' effect has the largest magnitude of any
term in con305 throughout much of the UT and at some points
is even larger than its counterpart in force300. At $\sim$239 K, the
q_i, q_i', ρ, and V_m effects all contribute equally to the increase in
$\dot{s}_{\text{ice}}$ in con305. This is in stark contrast to force300, in which only
the q_i and q_i' effects are significant. This has important implica-
tions for the latent heating efficiency, which is discussed in the
next section.

d. Latent heating efficiency

Having examined how $\dot{s}_{\text{ice}}$ changes in response to warming
SSTs and an imposed forcing, we can return to the question
posed at the end of section 2: why does the latent heating effi-
ciency ϵ increase with SST, and what can this tell us about the
q_i response to warming? Just as we did with $\dot{s}_{\text{ice}}$, we can
decompose changes in ϵ into contributions from the same six
variables (see appendix A). This decomposition is shown in
Fig. 6, which is restricted to the 215–245-K range over which ϵ
shows a clear dependence on SST. The ρ, Γ, V_m, and V_m' con-
tributions have been grouped into a single "non-q_i" term.
These non-q_i terms and q_i' have straightforward effects on ϵ:
wherever they act to increase s_{ice}, they also act to increase ϵ.
The q_i effect on ϵ is more complicated, since q_i appears both
explicitly and implicitly (via $\dot{s}_{\text{ice}}$) in Eq. (3). It can be shown
from (3) that

$$\frac{\partial\epsilon}{\partial q_i} = \frac{1}{L_s q_i^2}\left(q_i\frac{\partial\dot{s}_{\text{ice}}}{\partial q_i} - \dot{s}_{\text{ice}}\right) = \frac{k\Gamma V_m q_i'}{L_s \rho^{0.54} q_i^2}. \quad (11)$$

The algebraic signs on the right-hand side work out
such that $\partial\epsilon/\partial q_i$ takes the opposite sign of q_i'. Above the q_i
maximum at 234 K, q_i' is positive and so $\partial\epsilon/\partial q_i$ is negative,
meaning that ϵ will decrease in response to an increase in
cloud ice.

In force300, the total change in ϵ (solid black line in Fig. 6b) is
relatively small. Since the non-q_i contribution is also small, it
must then be the case that the q_i (green line) and q_i' (red line)
effects approximately cancel. Indeed, throughout most of the
temperature range shown in Fig. 6, the decrease in ϵ associated

with enhanced q_i is balanced by the increase associated with steeper q_i gradients.

On the other hand, ϵ increases significantly in con305. The non-q_i terms account for approximately half of the ϵ increase at high T but work against the increase at colder T. The rest of the ϵ change is explained by the q_i and q_i' effects, which differ significantly in shape from those in force300 because of the slight warming of the top of the q_i profile. To examine this effect, we shifted the con305 q_i profile toward colder temperatures by 1 K, which brings the top of the profile in line with that from con300. We then recalculated q_i' and ϵ at each T. The dotted black line in Fig. 6a shows the resulting $\Delta\epsilon$ profile, which is reduced in magnitude by ~50% or more compared to the actual con305 profile. This shows that approximately half of the ϵ increase in the UT can be explained by the warming of the convective layer top. At warmer temperatures, the non-q_i terms and warming of the convective layer top account for nearly all of the increase in ϵ from con300 to con305. At cold temperatures, where the non-q_i terms work against the ϵ increase, the rest is accounted for by the portions of the q_i and q_i' effects that are not associated with the temperature at the top of the convective layer.

The increase in ϵ with warming can be understood physically as a shortening of the residence time of ice (against sedimentation) at some particular temperature. This residence time can be expressed as $\tau_{\text{sed}} = -q_i/\dot{q}_{i_{\text{sed}}}$, where the negative sign converts the sedimentation tendency to a removal rate. Using Eqs. (2) and (3), it can be shown that $\tau_{\text{sed}} = \epsilon^{-1}$. When ϵ is high as in con305, ice is cycled through the upper troposphere at a faster rate, and the climatological q_i at any particular T is kept low by rapid sedimentation. On the other hand, when ϵ is low, ice lingers at a particular temperature for a greater amount of time before sedimenting onward to the next isotherm, and the same latent heating rate is associated with larger climatological q_i. It is important that this shortening of τ_{sed} with warming not be equated with an increase in the fall speed, which is only one of several factors that determine τ_{sed}.

The pattern of increasing ϵ and decreasing τ_{sed} with warming is supported by three additional model runs with SSTs of 295, 310, and 315 K, as shown in Fig. 7. Apart from their SSTs, these three runs have identical setups to con300 and con305.

5. Summary and discussion

This paper is motivated by the question of how the mean q_i in the tropical UT would respond to an increase in the radiative cooling rate. In our RCE simulations, the q_i response to warming SSTs is tempered by an increase in the latent heating efficiency ϵ, which allows con305 and force300 to achieve the same latent heating rate with different amounts of ice. The theoretical model developed in section 3 reveals that q_i is only one of several factors that determine $\dot{s}_{\text{ice}}$ and therefore ϵ. Applying this model to our simulations, we found that the increase in ϵ with warming can be explained primarily by 1) changes in the non-q_i terms and 2) the slight warming of the upper branch of the q_i profile. Another way to understand
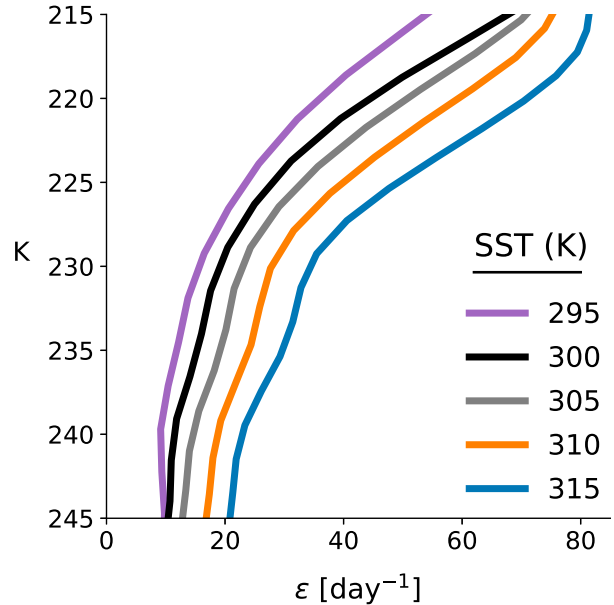

FIG. 7. Latent heating efficiency ϵ in the upper troposphere in RCE simulations with different SSTs.

these results is that ice is cycled across isotherms at a faster rate in con305 than in force300, and the lingering of ice at an isotherm in force300 results in a larger climatological q_i for a given latent heating rate. These results are summarized schematically in Fig. 8.

An important limitation of this work is that we have used only one model with one cloud microphysics scheme. Given the wide variety of cloud condensate profiles produced by the CRMs participating in RCEMIP (see Fig. 10c in Wing et al. 2020), it is likely that the q_i response to warming varies considerably across models. But our finding that ϵ increases with warming relies on some basic mechanisms that are widely supported by previous work, namely that SST warming causes a slight warming of the convective layer top and a decrease in ρ and Γ at fixed T. Barring drastic intermodel differences in the V_m response to warming, it is reasonable to suspect that the increase in ϵ with warming is robust. It would be beneficial to assess whether the RCEMIP models agree in this regard.

In this study, we have focused primarily on changes in the *domain-averaged* q_i because it can be theoretically linked to the energy balance requirements of RCE, as we have shown. But when it comes to global climate, changes in cloud amount and cloud optical properties with warming are of primary importance. In our RCE simulations, warming SSTs cause a reduction in cloud fraction and an increase in mean in-cloud q_i at fixed temperature (Fig. 3). Decreasing ice cloud area is consistent with the long-debated iris hypothesis (Lindzen et al. 2001) and the more recently developed stability iris hypothesis (Bony et al. 2016), both of which predict a reduction in anvil cloud fraction with warming. It is also in agreement with the majority of the cloud-resolving models in the RCEMIP ensemble (Wing et al. 2020). But it is important to recognize that a reduction in high cloud fraction is *not* an inevitable consequence of an increase
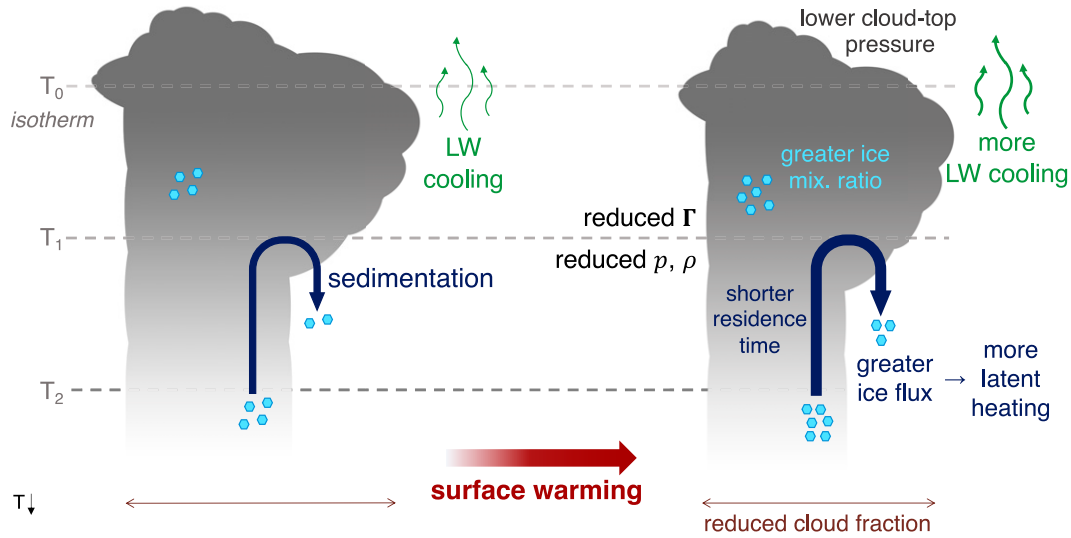
FIG. 8. Schematic diagram illustrating this paper's findings. (left) A cooler climate and (right) changes that occur with warming. Dashed gray lines are isotherms. The radiative cooling and latent heating rates at a fixed temperature level both increase. As isotherms rise to higher altitudes and lower pressures, the lapse rate Γ and ambient density ρ decrease. Clouds contain a greater amount of ice, but the residence time of ice at any particular temperature shortens. Cloud fraction decreases.

in ϵ or an increase in mean q_i. By themselves, increases in ϵ and q_i do not imply any specific changes in cloud amount or optical properties; because deep convection is associated with a variety of cloud types, there are myriad ways by which increases in ϵ and mean q_i could be achieved. The link between mean q_i and cloud fraction is further complicated by, among other factors, warming-induced changes in convective organization (Emanuel et al. 2014; Wing et al. 2017; Coppin and Bony 2018; Cronin and Wing 2017) and the complexity of anvil cloud dynamics (Schmidt and Garrett 2013; Hartmann et al. 2018; Gasparini et al. 2019; Wall et al. 2020).

Future work may focus on the extension of the framework developed here to three dimensions, which would reveal how changes in the mean ice amount and latent heating efficiency are manifested across the distribution of convective clouds. Recently, Beydoun et al. (2021) developed a diagnostic framework that is useful for interpreting changes in anvil cloud fraction. The integration of these two frameworks seems particularly promising and could advance understanding of the links between radiative cooling, latent heating, convection, and convective cloud cover.

Data availability statement. Output files from the model runs used in this study are available at http://hdl.handle.net/1773/46946. The model source code is publicly available.

APPENDIX A

Analytical Expressions for the Sensitivity of $\dot{s}_{ice}$ and ϵ

Here we provide expressions for the partial derivatives of $\dot{s}_{ice}$ on the right-hand side of Eq. (10). These expressions are derived from Eq. (9) and used to construct the curves shown in Fig. 3. The terms q_i' and V_m' denote $\partial q_i/\partial T$ and $\partial V_m/\partial T$, respectively. As an approximation, q_i and q_i' are treated as independent of one another, as are V_m and V_m'.

$$\frac{\partial \dot{s}_{ice}}{\partial \rho} = -0.54 \frac{\dot{s}_{ice}}{\rho},$$

$$\frac{\partial \dot{s}_{ice}}{\partial \Gamma} = \frac{k}{\rho^{0.54}} \left(\frac{0.46 V_m q_i}{T} - q_i V_m' - V_m q_i' \right),$$

$$\frac{\partial \dot{s}_{ice}}{\partial q_i} = \frac{k}{\rho^{0.54}} \left[\Gamma \left(\frac{0.46 V_m}{T} - V_m' \right) - \frac{0.46 c V_m}{T} \right],$$

$$\frac{\partial \dot{s}_{ice}}{\partial q_i'} = -\frac{k V_m \Gamma}{\rho^{0.54}},$$

$$\frac{\partial \dot{s}_{ice}}{\partial V_m} = \frac{k}{\rho^{0.54}} \left[\Gamma \left(\frac{0.46 q_i}{T} - q_i' \right) - \frac{0.46 c q_i}{T} \right],$$

$$\frac{\partial \dot{s}_{ice}}{\partial V_m'} = -\frac{k q_i \Gamma}{\rho^{0.54}}.$$
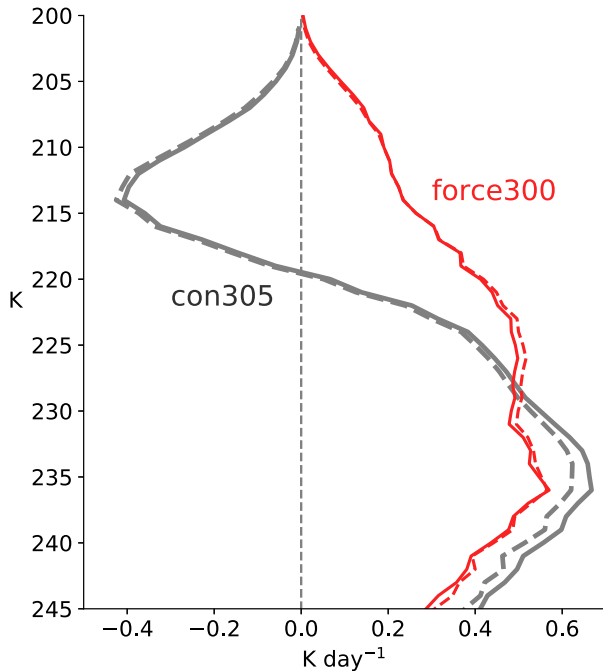
FIG. B1 . Change in $\dot{s}_{ice}$ relative to con300 calculated using Eq. (9) (solid lines) and the total differential approximation given by Eq. (10) (dashed lines).

In section 4d, $\Delta\epsilon$ is decomposed in the same manner as $\Delta\dot{s}_{ice}$. The total differential approximation for $\Delta\epsilon$, analogous to Eq. (10), is

$$\Delta\epsilon \approx \Delta\rho\,\frac{\partial\epsilon}{\partial\rho} + \Delta\Gamma\,\frac{\partial\epsilon}{\partial\Gamma} + \Delta V_m\,\frac{\partial\epsilon}{\partial V_m} + \Delta V'_m\,\frac{\partial\epsilon}{\partial V'_m}$$

$$+ \Delta q_i\,\frac{\partial\epsilon}{\partial q_i} + \Delta q'_i\,\frac{\partial\epsilon}{\partial q'_i}.$$

Using Eq. (3), $\partial\epsilon/\partial X$ can be expressed in terms of $\partial\dot{s}_{ice}/\partial X$ and evaluated using the expressions above, where X is ρ, Γ, q_i, q'_i, V_m, or V'_m. The results are used to construct the curves shown in Fig. 6.

APPENDIX B

Validation for the Total Differential Approximation for $\Delta\dot{s}_{ice}$

Here we validate the use of the total differential to assess changes in $\dot{s}_{ice}$. Figure B1 shows $\Delta\dot{s}_{ice}$ (relative to con300) for con305 and force300. The solid lines show the true change, calculated by evaluating Eq. (9) for each run and taking the difference at each T. Dashed lines show the approximate change given by the total differential [Eq. (10)]. For both con305 and force300, the total differential approximation is within 10% of the true change at all T with the exception of $T < 205$ K, where the fractional errors are slightly larger because $\Delta\dot{s}_{ice}$ is small in

magnitude. This close agreement validates the use of the total differential to attribute changes in $\dot{s}_{ice}$ to changes in other factors. The accuracy of the approximation is similar for changes in ϵ (not shown).

REFERENCES

Beydoun, H., P. M. Caldwell, W. M. Hannah, and A. S. Donahue, 2021: Dissecting anvil cloud response to sea surface warming. *Geophys. Res. Lett.*, **48**, e2021GL094049, https://doi.org/10.1029/2021GL094049.

Bony, S., and Coauthors, 2015: Clouds, circulation and climate sensitivity. *Nat. Geosci.*, **8**, 261–268, https://doi.org/10.1038/ngeo2398.

——, B. Stevens, D. Coppin, T. Becker, K. A. Reed, A. Voigt, and B. Medeiros, 2016: Thermodynamic control of anvil cloud amount. *Proc. Natl. Acad. Sci. USA*, **113**, 8927–8932, https://doi.org/10.1073/pnas.1601472113.

Coppin, D., and S. Bony, 2018: On the interplay between convective aggregation, surface temperature gradients, and climate sensitivity. *J. Adv. Model. Earth Syst.*, **10**, 3123–3138, https://doi.org/10.1029/2018MS001406.

Cronin, T. W., and A. A. Wing, 2017: Clouds, circulation, and climate sensitivity in a radiative-convective equilibrium channel model. *J. Adv. Model. Earth Syst.*, **9**, 2883–2905, https://doi.org/10.1002/2017MS001111.

Emanuel, K., A. A. Wing, and E. M. Vincent, 2014: Radiative-convective instability. *J. Adv. Model. Earth Syst.*, **6**, 75–90, https://doi.org/10.1002/2013MS000270.

Gasparini, B., P. N. Blossey, D. L. Hartmann, G. Lin, and J. Fan, 2019: What drives the life cycle of tropical anvil clouds? *J. Adv. Model. Earth Syst.*, **11**, 2586–2605, https://doi.org/10.1029/2019MS001736.

——, P. J. Rasch, D. L. Hartmann, C. J. Wall, and M. Dütsch, 2021: A Lagrangian perspective on tropical anvil cloud life-cycle in present and future climate. *J. Geophys. Res. Atmos.*, **126**, e2020JD033487, https://doi.org/10.1029/2020JD033487.

Grabowski, W. W., J.-I. Yano, and M. W. Moncrieff, 2000: Cloud resolving modeling of tropical circulations driven by large-scale SST gradients. *J. Atmos. Sci.*, **57**, 2022–2040, https://doi.org/10.1175/1520-0469(2000)057<2022:CRMOTC>2.0.CO;2.

Hartmann, D. L., 2016: Tropical anvil clouds and climate sensitivity. *Proc. Natl. Acad. Sci. USA*, **113**, 8897–8899, https://doi.org/10.1073/pnas.1610455113.

——, and K. Larson, 2002: An important constraint on tropical cloud–climate feedback. *Geophys. Res. Lett.*, **29**, 1951, https://doi.org/10.1029/2002GL015835.

——, B. Gasparini, S. E. Berry, and P. N. Blossey, 2018: The life cycle and net radiative effect of tropical anvil clouds. *J. Adv. Model. Earth Syst.*, **10**, 3012–3029, https://doi.org/10.1029/2018MS001484.

Heymsfield, A. J., G.-J. Zadelhoff, D. P. Donovan, F. Fabry, R. J. Hogan, and A. J. Illingworth, 2007: Refinements to ice particle mass dimensional and terminal velocity relationships for ice clouds. Part II: Evaluation and parameterizations of ensemble ice particle sedimentation velocities. *J. Atmos. Sci.*, **64**, 1068–1088, https://doi.org/10.1175/JAS3900.1.

Iacono, M. J., E. J. Mlawer, S. A. Clough, and J.-J. Morcrette, 2000: Impact of an improved longwave radiation model, RRTM, on the energy budget and thermodynamic properties of the NCAR Community Climate Model, CCM3. *J. Geophys. Res.*, **105**, 14 873–14 890, https://doi.org/10.1029/2000JD900091.

Jeevanjee, N., and D. M. Romps, 2018: Mean precipitation change from a deepening troposphere. *Proc. Natl. Acad. Sci. USA*, **115**, 11 465–11 470, https://doi.org/10.1073/pnas.1720683115.

——, and S. Fueglistaler, 2020: Simple spectral models for atmospheric radiative cooling. *J. Atmos. Sci.*, **77**, 479–497, https://doi.org/10.1175/JAS-D-18-0347.1.

Khairoutdinov, M. F., and D. A. Randall, 2003: Cloud resolving modeling of the ARM summer 1997 IOP: Model formulation, results, uncertainties, and sensitivities. *J. Atmos. Sci.*, **60**, 607–625, https://doi.org/10.1175/1520-0469(2003)060<0607:CRMOTA>2.0.CO;2.

Knutson, T. R., and S. Manabe, 1995: Time-mean response over the tropical Pacific to increased CO_2 in a coupled ocean–atmosphere model. *J. Climate*, **8**, 2181–2199, https://doi.org/10.1175/1520-0442(1995)008<2181:TMROTT>2.0.CO;2.

Lindzen, R. S., M. D. Chou, and A. Y. Hou, 2001: Does the Earth have an adaptive infrared iris? *Bull. Amer. Meteor. Soc.*, **82**, 417–432, https://doi.org/10.1175/1520-0477(2001)082<0417:DTEHAA>2.3.CO;2.

Lutsko, N. J., and T. W. Cronin, 2018: Increase in precipitation efficiency with surface warming in radiative-convective equilibrium. *J. Adv. Model. Earth Syst.*, **10**, 2992–3010, https://doi.org/10.1029/2018MS001482.

Mitchell, D. L., and A. J. Heymsfield, 2005: Refinements in the treatment of ice particle terminal velocities, highlighting aggregates. *J. Atmos. Sci.*, **62**, 1637–1644, https://doi.org/10.1175/JAS3413.1.

——, P. Rasch, D. Ivanova, G. McFarquhar, and T. Nousiainen, 2008: Impact of small ice crystal assumptions on ice sedimentation rates in cirrus clouds and GCM simulations. *Geophys. Res. Lett.*, **35**, L09806, https://doi.org/10.1029/2008GL033552.

Mitchell, J. F. B., and W. J. Ingram, 1992: Carbon dioxide and climate: Mechanisms of changes in cloud. *J. Climate*, **5**, 5–21, https://doi.org/10.1175/1520-0442(1992)005<0005:CDACMO>2.0.CO;2.

Mlawer, E. J., S. J. Taubman, P. D. Brown, M. J. Iacono, and S. A. Clough, 1997: Radiative transfer for inhomogeneous atmospheres: RRTM, a validated correlated-k model for the longwave. *J. Geophys. Res.*, **102**, 16 663–16 682, https://doi.org/10.1029/97JD00237.

Morrison, H., and J. A. Milbrandt, 2015: Parameterization of cloud microphysics based on the prediction of bulk ice particle properties. Part I: Scheme description and idealized tests. *J. Atmos. Sci.*, **72**, 287–311, https://doi.org/10.1175/JAS-D-14-0065.1.

——, ——, G. H. Bryan, K. Ikeda, S. A. Tessendorf, and G. Thompson, 2015: Parameterization of cloud microphysics based on the prediction of bulk ice particle properties. Part II: Case study comparisons with observations and other schemes. *J. Atmos. Sci.*, **72**, 312–339, https://doi.org/10.1175/JAS-D-14-0066.1.

Sanderson, B. M., C. Piani, W. J. Ingram, D. A. Stone, and M. R. Allen, 2008: Towards constraining climate sensitivity by linear analysis of feedback patterns in thousands of perturbed-physics GCM simulations. *Climate Dyn.*, **30**, 175–190, https://doi.org/10.1007/s00382-007-0280-7.

Schmidt, C. T., and T. J. Garrett, 2013: A simple framework for the dynamic response of cirrus clouds to local diabatic radiative heating. *J. Atmos. Sci.*, **70**, 1409–1422, https://doi.org/10.1175/JAS-D-12-056.1.

Sobel, A. H., J. Nilsson, and L. M. Polvani, 2001: The weak temperature gradient approximation and balanced tropical moisture waves. *J. Atmos. Sci.*, **58**, 3650–3665, https://doi.org/10.1175/1520-0469(2001)058<3650:TWTGAA>2.0.CO;2.

Sokol, A. B., and D. L. Hartmann, 2020: Tropical anvil clouds: Radiative driving toward a preferred state. *J. Geophys. Res. Atmos.*, **125**, e2020JD033107, https://doi.org/10.1029/2020JD033107..

Voigt, A., N. Albern, and G. Papavasileiou, 2019: The atmospheric pathway of the cloud-radiative impact on the circulation response to global warming: Important and uncertain. *J. Climate*, **32**, 3051–3067, https://doi.org/10.1175/JCLI-D-18-0810.1.

Wall, C. J., J. R. Norris, B. Gasparini, W. L. Smith, M. M. Thieman, and O. Sourdeval, 2020: Observational evidence that radiative heating modifies the life cycle of tropical anvil clouds. *J. Climate*, **33**, 8621–8640, https://doi.org/10.1175/JCLI-D-20-0204.1.

Wing, A. A., K. Emanuel, C. E. Holloway, and C. Muller, 2017: Convective self-aggregation in numerical simulations: A review. *Surv. Geophys.*, **38**, 1173–1197, https://doi.org/10.1007/s10712-017-9408-4.

——, and Coauthors, 2020: Clouds and convective self-aggregation in a multi-model ensemble of radiative-convective equilibrium simulations. *J. Adv. Model. Earth Syst.*, **12**, e2020MS002138, https://doi.org/10.1029/2020MS002138.

Zelinka, M. D., and D. L. Hartmann, 2010: Why is longwave cloud feedback positive? *J. Geophys. Res.*, **115**, D16117, https://doi.org/10.1029/2010JD013817.

——, and ——, 2011: The observed sensitivity of high clouds to mean surface temperature anomalies in the tropics. *J. Geophys. Res.*, **116**, D23103, https://doi.org/10.1029/2011JD016459.

——, S. A. Klein, and D. L. Hartmann, 2012: Computing and partitioning cloud feedbacks using cloud property histograms. Part I: Cloud radiative kernels. *J. Climate*, **25**, 3715–3735, https://doi.org/10.1175/JCLI-D-11-00248.1.

——, D. A. Randall, M. J. Webb, and S. A. Klein, 2017: Clearing clouds of uncertainty. *Nat. Climate Change*, **7**, 674–678, https://doi.org/10.1038/nclimate3402.

Zhou, W., and S.-P. Xie, 2019: A conceptual spectral plume model for understanding tropical temperature profile and convective updraft velocities. *J. Atmos. Sci.*, **76**, 2801–2814, https://doi.org/10.1175/JAS-D-18-0330.1.